Check for updates

ADVANCED FUNCTIONAL MATERIALS
www.afm-journal.de

Skin-Conformal Motion Monitoring Film for Deep-Learning-Based Immersive Extended Reality

Jihyeon Ahn, Taehwan Kim, Ji-Hwan Ha, Donho Lee, Osman Gul, Seokjoo Cho, Hyunjin Kim, Mingu Kang, Jungrak Choi, Junseong Ahn, and Inkyu Park**

Immersive technologies like virtual reality (VR) and augmented reality (AR) are rapidly advancing, but current motion tracking systems face significant limitations. Camera-based methods struggle with occlusion and environmental sensitivity, while existing skin-applied sensors suffer from poor adhesion or lack of reusability. This research introduces a deep-learning-based motion monitoring system utilizing a skin-conformal stretchable film for reliable and immersive motion tracking in VR and AR applications. The approach enhances skin adhesion through elastomer cross-linking weakening and microwrinkle formation. The developed skin-conformal motion monitoring film (SCMF) demonstrates 5.3 times higher skin adhesion (0.0218 N mm^{-1}) compared to conventional elastomer. With its improved adhesion, the SCMF demonstrates high conformality to skin movements, accurately following dynamic motions of the skin, resulting in reliable strain and bending angle signals. By applying the SCMF to finger joints, a system capable of reliably monitoring finger movements in a VR environment and classifying baseball grips using convolutional neural network (CNN) algorithms can be developed. The application is extended to 7 upper body parts, developing a real-time workout monitoring system in AR using change point detection and 2D CNN algorithms. The approach enhances accuracy and adaptability of motion tracking across immersive technologies, potentially transforming user experiences in various sectors.

1. Introduction

Immersive extended reality such as virtual reality (VR) and augmented reality (AR) has gained significant attention owing to the increase in remote work and non-face-to-face services, coupled with advancements in display and sensor technologies. By enabling users to experience a seamless integration of real and extended reality environments with enhanced immersion, these advancements play crucial roles in various sectors, including healthcare, education, and entertainment, facilitating economic and efficient development while connecting society without spatial or physical limitations.[1–3] Given their transformative potential, VR and AR technologies are expected to expand further into daily life and business operations, thereby accelerating technological advancements in the field. For applications requiring precise simulations or highly immersive experiences, such as medical training or deeply immersive entertainment, accurate synchronization between virtual and real worlds is essential. Thus, the efficacy of immersive technologies heavily relies on precise tracking of real-world motion in the virtual environment. Currently, the industry predominantly utilizes camera-based tracking methods for capturing subtle movements and gestures. However, camera-based systems are subject to limitations such as dependency on camera positioning, potential occlusion issues, and sensitivity to environmental light conditions. Additionally, the high cost of motion tracking cameras poses accessibility challenges for general consumers. In response to the limitations of camera-based systems, researchers have intensified efforts to explore both alternative and complementary tracking methods. Recent investigations have particularly focused on integrating motion sensors, aiming to overcome the constraints inherent in traditional camera-based approaches.[4–7] Motion monitoring sensors offer potential solutions by maintaining tracking accuracy regardless of environmental conditions or providing cost-effective alternatives to camera-based systems.[8–10] For example, some studies have explored smart gloves for VR and AR applications,[11] but their accuracy still vary depending on the fit to individual hand sizes, and they are limited to capturing only hand movements.[11,12] Previous research on

J. Ahn, T. Kim, D. Lee, O. Gul, S. Cho, H. Kim, M. Kang, J. Choi, I. Park
Department of Mechanical Engineering
Korea Advanced Institute of Science and Technology (KAIST)
Daejeon 34141, Republic of Korea
E-mail: inkyu@kaist.ac.kr
J.-H. Ha
Center for Nano Lithography & Manufacturing
Korea Institute of Machinery and Materials (KIMM)
Daejeon 34103, Republic of Korea
J. Choi
Electronics and Telecommunications Research Institute (ETRI)
Daejeon 34129, Republic of Korea
J. Ahn
Department of Control and Instrumentation Engineering
Korea University
Sejong 30019, Republic of Korea
E-mail: junseong@korea.ac.kr

The ORCID identification number(s) for the author(s) of this article can be found under https://doi.org/10.1002/adfm.202502568

DOI: 10.1002/adfm.202502568

 © 2025 Wiley-VCH GmbH

alternative form factors, such as skin-printed type[13–16] or skin-attached type[17–30] sensors applied directly to the skin for motion tracking, can potentially be adapted for immersive technology applications. However, each of approaches has its own limitations. Skin-printed type sensors, although highly conformable to the skin, are typically not reusable, which can be impractical for long-term or repeated use. Conversely, skin-attached type sensors offer a durable solution, but poor adhesion to the skin can lead to delamination during dynamic motions, potentially compromising tracking accuracy in immersive applications.[17] To address these issues of skin-attached type sensors, integrating machine learning (ML) and deep learning (DL) with sensors for improving accuracy has been explored.[31,32] However, the lack of reliable sensor hardware limits the effectiveness of learning algorithms. As a result, previous VR and AR systems can only monitor discrete predefined gestures or motions rather than continuous motion monitoring.[11,33] Therefore, it is crucial to develop an integrated system that combines reliable sensor hardware with software capable of real-time motion monitoring in VR and AR environments, advancing both sensor and the corresponding ML/DL and VR/AR systems together.

This research introduces a reusable skin-conformal motion monitoring film (SCMF) that, like a skin-printed type, possesses high adhesion for applications in immersive technologies. Furthermore, a system integrating the SCMF with ML/DL algorithms and VR/AR environments was developed, enabling real-time acquisition and representation of motion data. The SCMF consists of multiple layers including an adhesive layer, conductive layers, and a dielectric layer, designed to measure capacitance changes corresponding to strain and bending angles. The adhesive layer, which directly interfaces with the skin, plays a crucial role in achieving the skin-conformal properties of the film. Characteristic tests of the film demonstrated its ability to measure capacitance signal changes corresponding to strain and bending angles. When applied to the skin, the SCMF adheres conformally during movement, allowing for reliable sensing of strain in areas such as the calf and forearm, as well as joint angles of the elbow, shoulder, and wrist. To validate the SCMF's performance and demonstrate its versatility, the film was applied to multiple body locations and integrated into both VR and AR systems. In a VR scenario, the SCMF was applied to finger joints to track hand movements and classify different gestures, such as baseball pitching grips. For an AR application, the film was used on 7 upper body locations including chest and shoulders to monitor workout movements. Both applications utilized deep learning algorithms for accurate motion classification and real-time feedback, showcasing the SCMF's potential in fields such as entertainment, healthcare, and fitness monitoring.

2. Results and Discussion

2.1. Overview of SCMF for Immersive Extended Reality

This research introduces a wearable SCMF designed to adhere to joints and skin, enabling precise tracking of strain and bending angle (**Figure 1a**). The SCMF monitors motion by sensing changes in capacitance that occur with movement. It is designed with two conductive layers and one dielectric layer between them, along with an adhesive layer on the base to ensure adhesion to the skin. The adhesive layer was fabricated by incorporating polyethyleneimine ethoxylated (PEIE) into an elastomer matrix (Figure 1b). The incorporation of PEIE into the elastomer matrix weakens the cross-linking within the elastomer, while simultaneously promoting the formation of microwrinkles on the film surface. The weakened cross-linking and microwrinkles contribute to the SCMF's high skin conformality, allowing it to maintain high adhesion with the skin even during concave motions, such as wrist extension. Notably, the film exhibits consistent deformation during repetitive bending and stretching motions, resulting in highly reproducible signals. Additionally, the high adhesion prevents unintended deformations caused by detachment from the skin, reducing unexpected noise. As a result, the signal-to-noise ratio (SNR) improves, enhancing the reliability and decreasing its limit of detection (LOD). The advancements enable the measurement of subtle strain variations, such as those in forearm muscles during wrist movements. The improved reliability and LOD establish effectively capturing both joint bending motions and skin strain changes, forming a robust foundation for the VR and AR motion monitoring system developed.

To exhibit the SCMF's capabilities in VR applications, the film was attached to five finger joints (Figure 1c(i)). The data obtained from finger movements were processed for calibration using a simple artificial neural network (ANN) algorithm. The calibrated data were then integrated into a VR environment, enabling real-time replication of hand movements on a virtual hand model. Then, a VR baseball game was implemented that classifies pitcher's grips (knuckleball, fastball, changeup) using a 1D convolutional neural network (CNN) algorithm applied to the SCMF data from the user's hand.

The SCMF's application was subsequently expanded to AR systems. For the expansion, the film was applied to 7 upper body locations, including the chest, wrists, elbows, and shoulders on both sides (Figure 1c(ii)). The configuration allowed for real-time visualization of joint angles and strain rates during motion in an AR application. A change point detection and 2D CNN algorithm were implemented to automatically classify workout types (arm curl, shoulder press, side lateral raise) based on data from four films after each workout cycle. Furthermore, the system provides immediate feedback on workout type and form for each joint through the AR application. The integration enables users to observe their movements while simultaneously receiving real-time data on joint and strain changes, along with instantaneous feedback, creating a comprehensive motion monitoring and analysis system for fitness applications.

2.2. SCMF's Adhesive Layer: Mechanisms and Characteristics of Adhesion

Figure 2 illustrates the adhesion mechanism and characteristics of the SCMF's adhesive layer. The incorporation of PEIE into the elastomer precursors results in phase separation due to their disparate properties.[34] Phase separation creates an inhomogeneous distribution of PEIE, forming discrete regions within the elastomer matrix rather than a uniform blend. The resulting structure exhibits a nonuniform composition at the microscopic level prior to curing, with PEIE dispersed in localized areas throughout the elastomer. In the regions where PEIE is mixed

© 2025 Wiley-VCH GmbH

16163028, 2025, 28, Downloaded from https://advanced.onlinelibrary.wiley.com/doi/10.1002/adfm.202502568 by Korea University Medical, Wiley Online Library on [21/07/2025]. See the Terms and Conditions (https://onlinelibrary.wiley.com/terms-and-conditions) on Wiley Online Library for rules of use; OA articles are governed by the applicable Creative Commons License

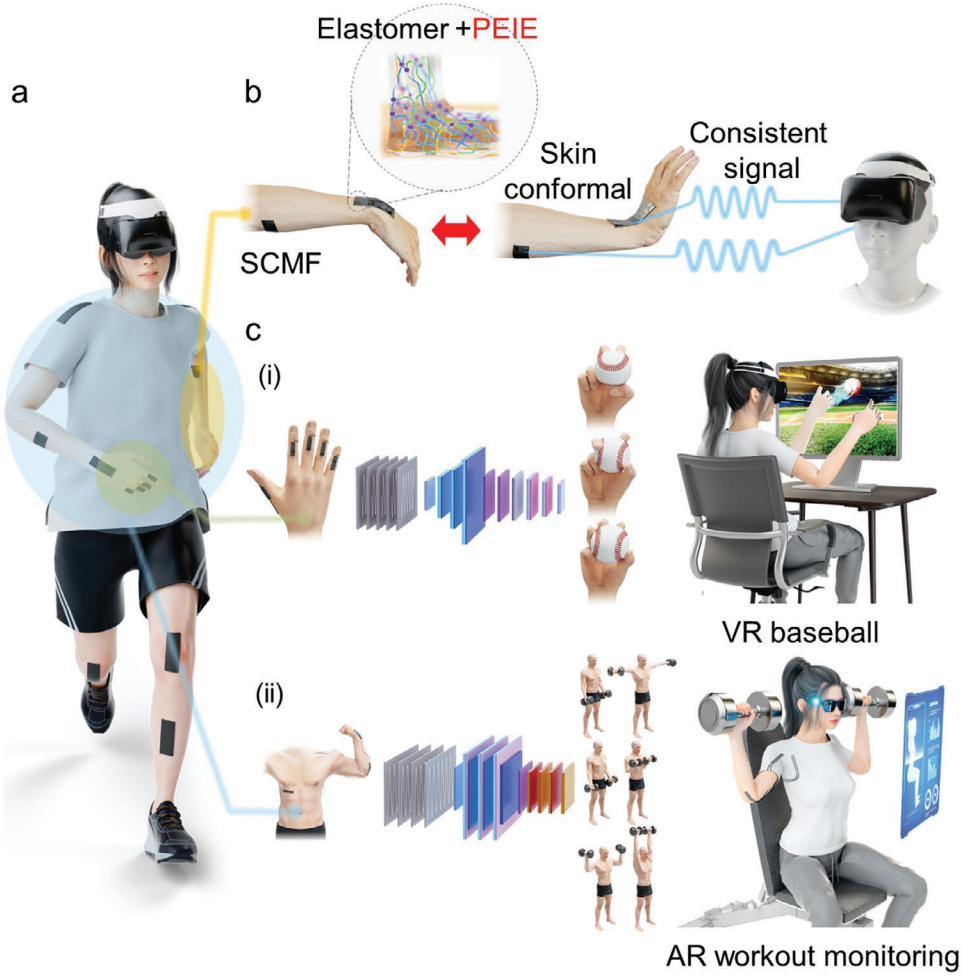


Figure 1. Concept and implementation of skin-conformal-motion-monitoring-film (SCMF)-based motion tracking for immersive VR and AR systems. a) Illustration showing the application of the SCMF on the body during physical activities. b) As the body moves consistently, the SCMF remains conformally attached to the forearm and wrist, capturing reliable signals that are transmitted to VR and AR platforms. c) Applications using the sensor. i) VR baseball game system: films are attached to all five fingers, and the grip types of a baseball are classified using a CNN. The classified grips are then visualized in a VR environment. ii) Workout monitoring system: seven films are placed on the upper body, classifying different exercises using CNN. The classified exercise types are provided as real-time feedback through an AR application, enhancing the workout experience.

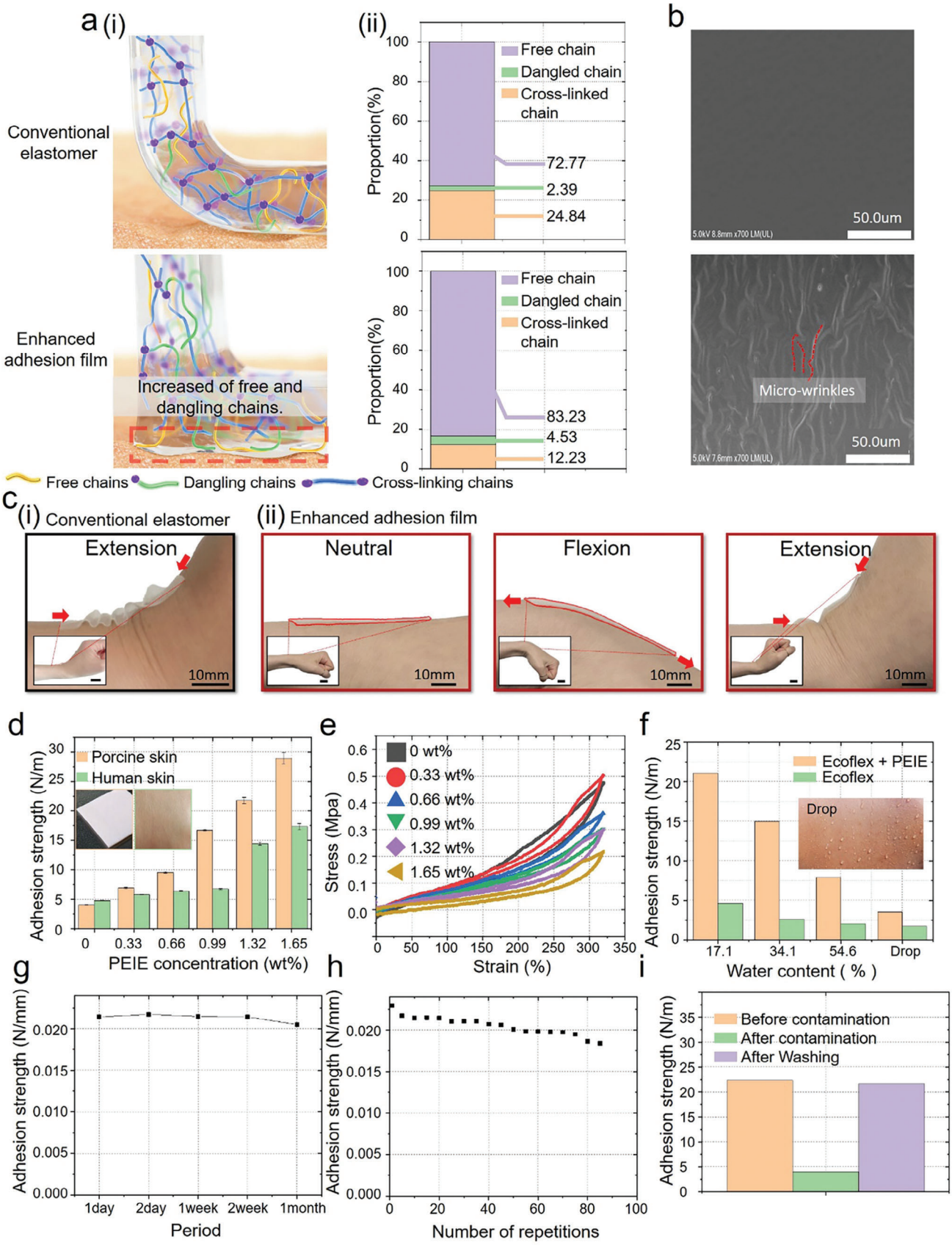
with the elastomer, the amine groups (H—N—H) in PEIE interact with the siloxane (Si—O—Si) network of the elastomer, weakening the cross-linking within the elastomer structure. The nonuniform cross-linking density of elastomer significantly enhances the film's adhesion to substrates through two primary mechanisms in the following text.

First, the weakening of cross-linking results in an increased proportion of free chains on the material surface (Figure 2a(i) and Figure S1 (Supporting Information)). Quantitative analysis using nuclear magnetic resonance (NMR) spectroscopy reveals that the ratio of free chains to cross-linked chains is significantly higher in the enhanced adhesion film (6.64) compared to the conventional elastomer (2.93) (Figure 2a(ii)). Free chains, characterized by their complete absence of cross-linking points, exhibit enhanced molecular mobility that enables migration to the substrate interface where they facilitate robust adhesion through physical entanglement mechanisms. Dangling chains, tethered at a single point, maintain sufficient conformational freedom to maximize interfacial contact area. Cross-linked chains, featuring multiple covalent junction points, form an interconnected 3D network that provides mechanical strength and elasticity to the system.[35,36] The increased free chain content in the enhanced film directly contributes to its improved adhesive properties.[37] The film's heterogeneous structure maintains regions of high cross-linking density alongside areas of weakened cross-linking, allowing the film to preserve good resilience and durability while simultaneously enhancing adhesion. Second, the heterogeneous cross-linking density distribution leads to stress concentration during the curing process, resulting in the formation of microwrinkles (Figure 2b). The microwrinkles (with widths of hundreds of nanometers) on the film, despite being much smaller than natural skin wrinkles (with widths ranging from tens to hundreds of micrometers), enhance adhesion by increasing surface area and promoting stronger van der Waals interactions. When soft skin comes into contact with a soft microwrinkled elastomer, it conforms to the shape of the elastomer. As a result, the

 © 2025 Wiley-VCH GmbH

16163028, 2025, 28, Downloaded from https://advanced.onlinelibrary.wiley.com/doi/10.1002/adfm.202502568 by Korea University Medical, Wiley Online Library on [21/07/2025]. See the Terms and Conditions (https://onlinelibrary.wiley.com/terms-and-conditions) on Wiley Online Library for rules of use; OA articles are governed by the applicable Creative Commons License

16163028, 2025, 28, Downloaded from https://advanced.onlinelibrary.wiley.com/doi/10.1002/adfm.202502568 by Korea University Medical, Wiley Online Library on [21/07/2025]. See the Terms and Conditions (https://onlinelibrary.wiley.com/terms-and-conditions) on Wiley Online Library for rules of use; OA articles are governed by the applicable Creative Commons License



© 2025 Wiley-VCH GmbH

16163028, 2025, 28, Downloaded from https://advanced.onlinelibrary.wiley.com/doi/10.1002/adfm.202502568 by Korea University Medical, Wiley Online Library on [21/07/2025]. See the Terms and Conditions (https://onlinelibrary.wiley.com/terms-and-conditions) on Wiley Online Library for rules of use; OA articles are governed by the applicable Creative Commons License

contact area increases proportionally to the expanded surface area of the elastomer.[38,39] Remarkably, the microwrinkles conform well to the skin's surface, improving contact and adhesion without being affected by the size difference between the microwrinkles and natural skin wrinkles.

The high adhesion properties make film particularly suitable for wearable motion monitoring applications where reliable signal acquisition is crucial. Highly reliable signals enable precise calibration and enhance the performance of deep learning algorithms, leading to improved motion classification accuracy. The significance of enhancing the film's adhesion becomes apparent when it is attached to the skin during concave motions. As the skin bends, it forms wrinkles that push against the film. The pushing force can cause the film to start peeling away from the skin, potentially disrupting adhesion. While conventional elastomers often detach from the skin during these challenging movements (Figure 2c(i)), the film's enhanced adhesion characteristics enable it to maintain consistent skin contact throughout various motions such as flexion, extension, and twisting (Figure 2c(ii) and Figure S2 (Supporting Information)). Quantitative adhesion force measurements were conducted using peel tests on both human and porcine skin (Figure 2d and Figure S3 (Supporting Information)). Higher PEIE concentrations led to increased adhesion force due to more extensive weakening of cross-linking and enhanced microwrinkle formation. To evaluate the film's ability to return to its original shape after repeated motions, hysteresis tests were conducted (Figure 2e). As the PEIE concentration increased, a corresponding rise in hysteresis was observed. While the formulation exhibited a 9.24% hysteresis at 100% strain, further increases in PEIE concentration resulted in a significant rise in hysteresis, reaching 62.19%, compared to 6.53% for the conventional elastomer (Figure S4, Supporting Information). The relationship between network structure modification and mechanical properties was systematically investigated. The reduced cross-linking density from PEIE incorporation resulted in increased chain mobility, which enhanced adhesion but led to greater energy dissipation during deformation. Through systematic optimization considering the requirements for wearable applications, where both high adhesion and mechanical reliability are crucial, 1.32 wt% PEIE was identified as the optimal concentration. The selected film demonstrated an adhesion force of 0.0218 N mm^{-1}, 5.3 times higher than conventional elastomer with 0 wt% PEIE, while also possessing a low modulus of 0.052 MPa and high stretchability (664%), allowing it to conformally follow skin movements (Figure S5, Supporting Information).

The film's reusability was evaluated through adhesion tests under both contamination and repeated use. Peel tests were conducted to assess the effect of moisture content on adhesion force, simulating the impact of perspiration (Figure 2f). While adhesion force decreased with increasing water content absorbed by the porcine skin due to interference with skin interactions, the film maintained 3.9 times higher adhesion force compared to conventional elastomer for up to ≈50% moisture content.[40] To further evaluate the performance under real-world conditions, sweat-induced measurements were conducted during exercise. Signal measurements before and after exercise demonstrated reliable motion detection capabilities even under sweating conditions (Figure S6, Supporting Information), with detailed experimental procedures provided in the Experimental Section. While sweating slightly weakened the adhesion, it had minimal impact on the motion sensing capabilities of the device, confirming the SCMF's reliability under real-world conditions. Notably, peel tests conducted at different skin pH conditions (pH 4–6) showed no significant variation in adhesion performance, demonstrating stable attachment across typical skin pH ranges (Figure S7, Supporting Information). Furthermore, to evaluate the long-term reusability of the SCMF, tests were conducted to assess its performance over extended periods. The film maintained its high adhesion even after one month following sensor fabrication (Figure 2g). Additionally, the film retained high adhesion even after 90 cycles of attachment and detachment (Figure 2h) and could be cleaned and reused after dust contamination (as described in the Experimental Section) by using a brief 10 min sonication in ethanol (Figure 2i and Figure S8 (Supporting Information)). These results demonstrate the SCMF's enhanced adhesion and reusability, highlighting its potential for reliable, long-term use in wearable motion monitoring applications, offering advantages over conventional adhesives (Figure S9 and Table S1, Supporting Information).

2.3. SCMF Fabrication and Characterization: Strain and Bending Angle Response

The SCMF was fabricated using the previously developed high-adhesive film as its base, incorporating a capacitance-type sensing mechanism. The capacitance-type approach is stable against environmental factors such as temperature and humidity (Figure S10, Supporting Information). For the conductive layers, carbon nanotubes (CNTs), known for chemical stability, lightweight, and high conductivity, were selected. Spray coating was employed

Figure 2. Adhesion mechanisms and characteristics. a) i) Schematic comparison of chain distribution between conventional elastomer and the enhanced adhesion elastomer film using PEIE. The conventional elastomer has a higher number of cross-linked chains near the substrate, which limits adhesion, whereas the enhanced adhesion film features a greater number of free chains and dangled chains, significantly enhancing its adhesion. ii) Quantitative NMR data comparing the chain mobility of conventional elastomer and the enhanced adhesion film. b) Scanning electron microscope (SEM) images showing the surface morphology of conventional elastomer (without wrinkles) and the enhanced adhesion film (with numerous microwrinkles). c) Visual comparison during wrist flexion and extension: the conventional elastomer shows delamination, failing to follow the skin's contours (i), while the enhanced adhesion elastomer maintains strong adhesion and conforms to the skin's wrinkles during extension (ii). d) Peel test results on porcine and human skin comparing adhesion strength across different PEIE concentrations, demonstrating superior adhesion with higher PEIE levels in the enhanced adhesion elastomer. e) Stress–strain curves comparing hysteresis for various PEIE concentrations, highlighting the balance of elasticity and adhesion in the enhanced adhesion elastomer. f) Peel test results on porcine skin under varying moisture levels to simulate the impact of sweat, showing the adhesion performance of the enhanced adhesion elastomer compared to conventional elastomer. g) Test for adhesion degradation over time after the film was fabricated. h) Adhesion strength data after repeated attachment and peeling processes up to 90 cycles. i) Comparison of adhesion strength before contamination, after contamination with dust, and after cleaning with a sonicator and ethanol.

 © 2025 Wiley-VCH GmbH

16163028, 2025, 28, Downloaded from https://advanced.onlinelibrary.wiley.com/doi/10.1002/adfm.202502568 by Korea University Medical, Wiley Online Library on [21/07/2025]. See the Terms and Conditions (https://onlinelibrary.wiley.com/terms-and-conditions) on Wiley Online Library for rules of use; OA articles are governed by the applicable Creative Commons License

to deposit CNTs as thin, uniform layers of ≈5 µm thickness, as excessive thickness can lead to crack formation and conductivity loss during mechanical stretching. The CNTs were subsequently embedded in an elastomer matrix during curing, ensuring secure integration and enabling unified deformation without delamination.[41,42] The potential effects of this fabrication process on the CNTs were investigated through Raman spectroscopy analysis, comparing the characteristics before and after processing, as shown in Figure S11 (Supporting Information).[43] The dielectric layer, situated between the conductive layers, was created by spin-coating a thin layer of Ecoflex (**Figure 3a**). The operating principle of the film involves a multiscale mechanisms: at macro- and microscales, when strain is applied, the dielectric layer undergoes both vertical compression and lateral expansion following the Poisson effect, resulting in thickness reduction. At the nanoscale, the CNT network in the conductive layers maintains continuous pathways during deformation, enabling a linear change in capacitance (Figure S12, Supporting Information).[44] The SCMF's capacitance-based sensing capabilities and performance under various conditions were demonstrated by analyzing its response to uniaxial strain. Figure 3b illustrates the capacitance change $(C - C_0)/C_0$ of the SCMF in response to applied strain, with a strain range of 0–100%. The SCMF demonstrates a gauge factor of 0.274 and linearity ($R^2 = 0.9998$) even at low strain levels (Figure S13, Supporting Information). Additionally, for three loading and unloading cycles of the SCMF in the strain range of 0–100%, the average hysteresis is as low as 0.0030 (Figure 3c). Subsequently, the dynamic response of the SCMF was evaluated. Figure 3d and Figure S14 (Supporting Information) demonstrate the stable dynamic response of the SCMF for strain ranges from $\varepsilon = 0\%$ to $\varepsilon = 50\%$. Furthermore, Figure 3e shows the step response with a strain step of 1%. Notably, the SCMF accurately responds to strains below 1% (Figure S15, Supporting Information). In addition, the response and recovery times of the SCMF were examined. Figure 3f shows that when 100% strain is applied to the film, the response and recovery times are 3.11 and 16.7 ms, respectively (Figure S16, Supporting Information). To evaluate durability, a cycle test with 100% strain was conducted for up to 40 000 cycles (Figure 3g and Figure S17 (Supporting Information)). The SCMF demonstrated long-term stability, with the capacitance changing only slightly by 0.66% after 40 000 cycles compared to the first cycle. To demonstrate the SNR in wearable applications, Figure 3h compares the SNR at 50% strain without and with hand proximity. The SNR values were 525.1 and 103.0, respectively, confirming that strain-induced capacitance changes can be accurately measured even under the influence of hand capacitance noise. Additionally, the SCMF demonstrates an extremely low LOD of 0.014% strain. Comparison of responses from four films of identical size, fabricated through identical processes, revealed a low sample to sample variation with an average variation of 0.570% (Figure 3i and Figure S18 (Supporting Information)). The stability and reliability enable the use of multiple films in the same system while maintaining data coherence. Moreover, the low variation enhances the scalability of the system and facilitates reliable comparative analysis across different body parts or individuals.

Additionally, when applied to the skin for wearable motion monitoring, the SCMF experiences strain during joint bending, resulting in changes to its capacitance. The measured capacitance values demonstrate a linear relationship with the joint bending angle (∅), expressed as $\frac{\Delta C}{C_0} = (h + a)\frac{\emptyset}{L_0}$ (Figure 3j and Note S1 (Supporting Information)),[45] where h is the dielectric thickness, a is the radius of curvature, and L_0 is the initial length. Testing the SCMF's response to bending while fixed to a substrate, simulating wearable use, revealed high linearity ($R^2 = 0.996$) between capacitance change and bending angle at a constant bending rate (Figure 3k). Figure 3l shows the SCMF's bending–relaxing cycles over 1000 repetitions. The signal difference was only 1.08% after 1000 cycles, indicating its stability under bending condition. The detailed experimental setup is provided in Figure S19 (Supporting Information).

2.4. SCMF Characterization as a Wearable Motion Monitoring Film: Strain and Bending Angle Response across Various Body Parts

To evaluate the SCMF's performance as wearable application, characteristic tests were conducted by attaching it to various body parts (**Figure 4**). Figure 4a illustrates a comparison between a conventional elastomer-based motion monitoring film and the SCMF. Both were attached to the wrist and subjected to repetitive up-and-down bending motions to compare signal reliability. Despite consistent wrist movements, the conventional elastomer-based film failed to adhere properly, resulting in unintended deformation and unreliable signals (Figure 4a(i)). By contrast, the SCMF exhibited reliable output, accurately reflecting the consistent wrist movements (Figure 4a(ii)). Given the reliability, the SCMF was attached to multiple body locations including fingers, elbows, shoulders, biceps, forearms, and calves to demonstrate its potential for comprehensive human motion detection. Figure 4b and Figure S20 (Supporting Information) demonstrate the SCMF's response to changes in finger bending. The film accurately captured 10° step increases in bending angle, demonstrating its ability to detect finger joint movements. Figure 4c,d along with Figure S21 (Supporting Information) displays response curves of the film related to elbow and shoulder joint bending, demonstrating reliable signals. Furthermore, when measuring strain on various body parts, the film remained securely in place without slipping or twisting, enabling the acquisition of distinct signals with low LOD. The film's capability was demonstrated by attaching it to the biceps during arm flexion, the forearm during wrist movements, and the calf during ankle rotations (Figure 4e–g). The SCMF successfully monitored minor skin deformations resulting from such subtle muscle movement.

2.5. Application to VR: Baseball Pitcher Grip Classification

Immersive technologies are extensively utilized in the entertainment industry due to their ability to create a highly engaging and interactive user-environment experience. To demonstrate SCMF's potential in the field, a VR baseball pitcher grip classification system was developed. The SCMF and circuit board were connected via wire, and the effects of stray capacitance from this board–wire configuration were demonstrated in Figure S22 (Supporting Information). The developed system monitors hand movements and classifies different types of baseball

 © 2025 Wiley-VCH GmbH

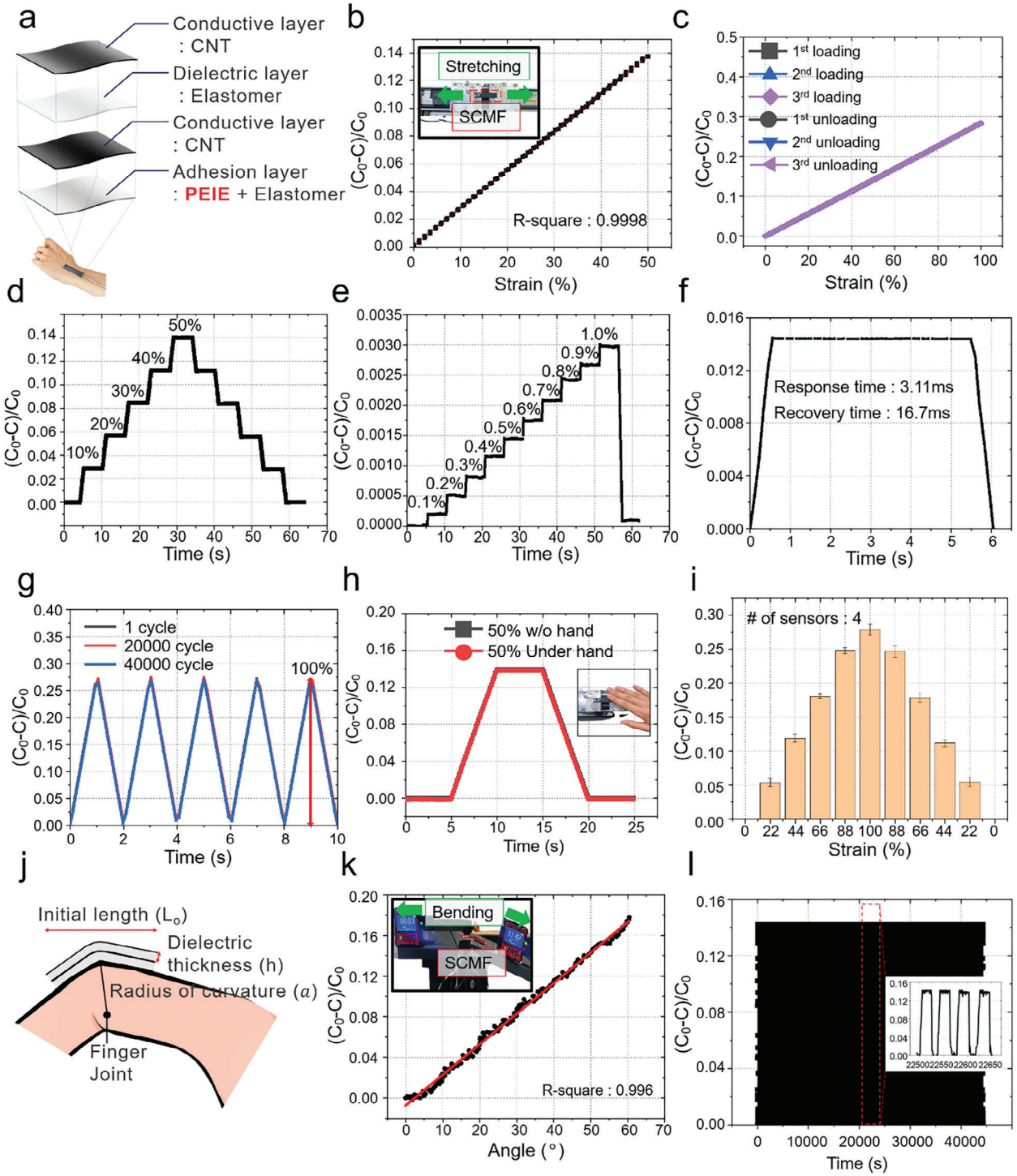


Figure 3. SCMF structure and performance characteristics. a) Layer-by-layer structure of the SCMF. b) Linearity test of the SCMF showing the capacitance response when 50% strain is applied at a rate of 10% s^{-1}. The inset shows the experimental setup. c) Response of the SCMF during three loading and unloading cycles with 100% strain applied at a rate of 10% s^{-1}. d) Dynamic test response of the SCMF when strain is incrementally increased by 10% up to 50% at a rate of 10% s^{-1}. e) Response of the SCMF when strain is incrementally increased by 0.1% up to 10% at a rate of 10% s^{-1}. f) Response time of the SCMF during loading and unloading when 100% strain is applied and then released back to 0%. g) Results of a long-term cycle test with 40 000 cycles of 100% strain loading and unloading. The comparison of the response after 1, 20 000, and 40 000 cycles is shown. h) Comparison of SNR values with and without the influence of hand capacitance on the SCMF. i) Sample-to-sample variation in capacitance response to strain across four SCMF sensors. j) Schematic showing the capacitance change of the SCMF as a function of bending angle when attached to a joint. k) Linear capacitance response of the SCMF as a function of bending angle, up to 50°. The inset shows the experimental setup. l) Response of the SCMF during a long-term cycle test with 1000 cycles of repeated bending up to 50°.

© 2025 Wiley-VCH GmbH

16163028, 2025, 28, Downloaded from https://advanced.onlinelibrary.wiley.com/doi/10.1002/adfm.202502568 by Korea University Medical, Wiley Online Library on [21/07/2025]. See the Terms and Conditions (https://onlinelibrary.wiley.com/terms-and-conditions) on Wiley Online Library for rules of use; OA articles are governed by the applicable Creative Commons License

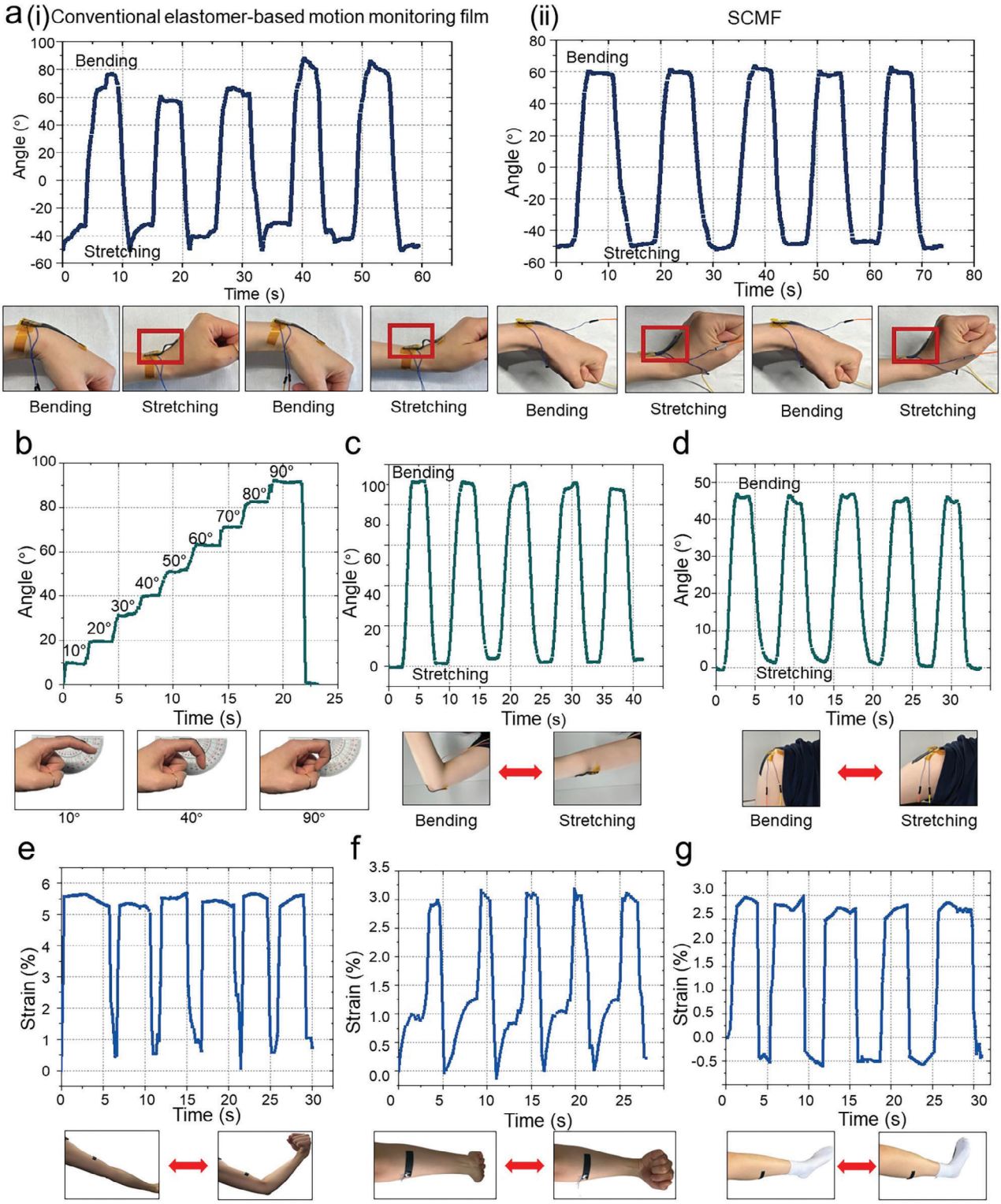


Figure 4. SCMF performance characteristics in diverse body motion detection. a) Response during consistent bending and stretching of the wrist. i) Unreliable response of conventional elastomer-based motion monitoring film. ii) Reliable signal from SCMF. b–g) Response of SCMF attached to various body parts during motions. (b) Finger angle response of SCMF when attached to a finger and bent in 10° increments. (c) Elbow angle response when SCMF is attached to the elbow and repeatedly bent and extended. (d) Shoulder angle response signal when SCMF is attached to the shoulder and moved. (e) Strain signal of the bicep when SCMF is attached and the arm is bent and extended. (f) Measurement of strain changes in the forearm muscle when SCMF is attached and the wrist is repeatedly bent and extended. (g) Strain signal of the calf muscle when SCMF is attached and the foot is tapped.

© 2025 Wiley-VCH GmbH

16163028, 2025, 28, Downloaded from https://advanced.onlinelibrary.wiley.com/doi/10.1002/adfm.202502568 by Korea University Medical, Wiley Online Library on [21/07/2025]. See the Terms and Conditions (https://onlinelibrary.wiley.com/terms-and-conditions) on Wiley Online Library for rules of use; OA articles are governed by the applicable Creative Commons License

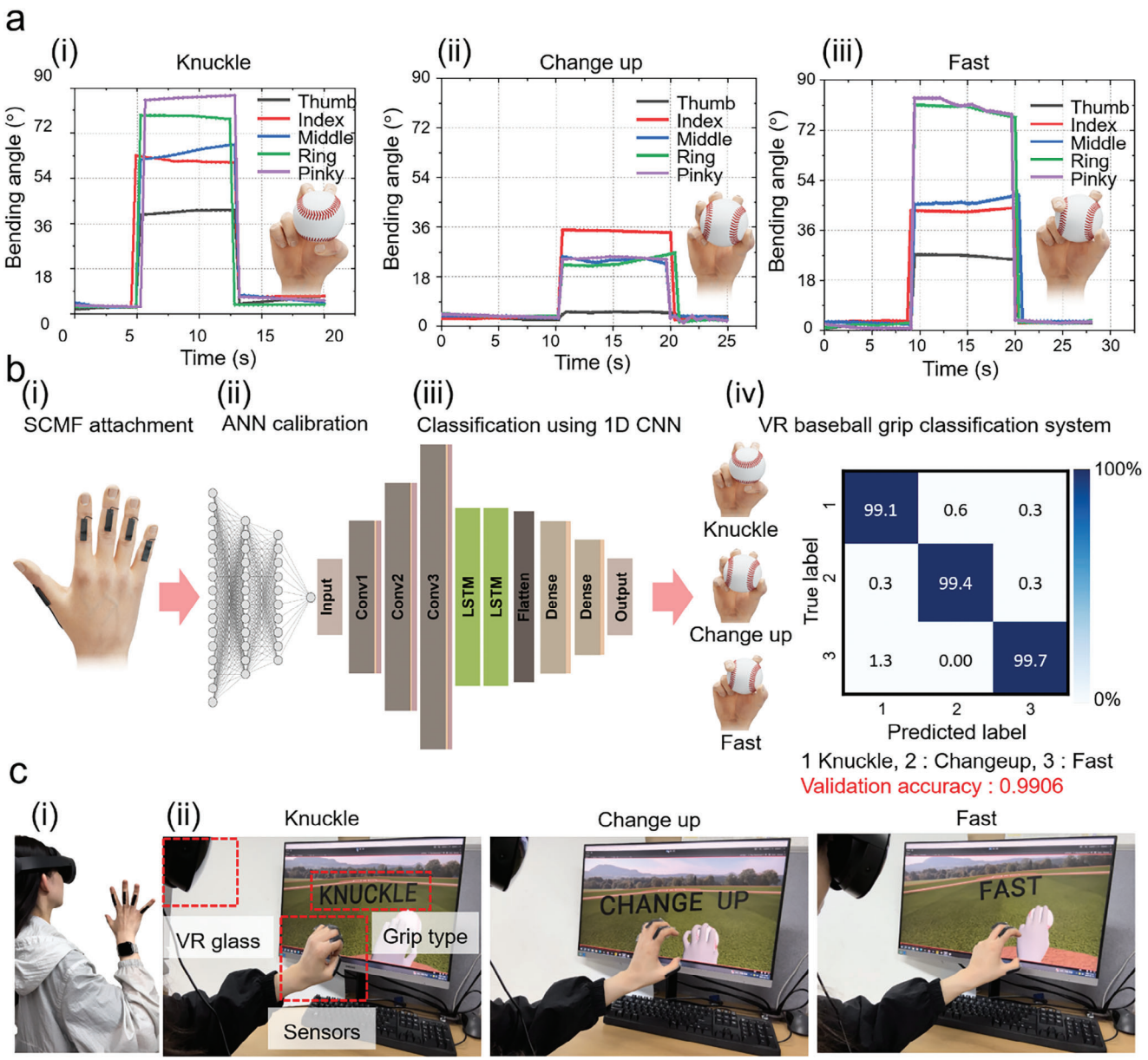


Figure 5. Demonstration of SCMF application for baseball grip classification in VR. a) Grip configuration for i) knuckleball, ii) changeup, and iii) fastball, along with SCMF signals recorded from each finger while holding the grips. b) Overview of a VR baseball grip classification system. i) Attaching SCMF to all five fingers. ii) ANN linear calibration of SCMF signals. iii) CNN architecture for classification of knuckleball, changeup, and fastball grips. iv) Confusion matrix of the classification results, with a validation accuracy of 0.9906. c) Photos demonstrating the system. i) A user wearing VR glasses and SCMF on all five fingers. ii) Demonstration of the system, showing finger movements and classification results for three grip types within the VR environment.

grips in a VR environment, enabling virtual pitching simulation. **Figure** 5a illustrates the three main types of grips analyzed – knuckleball, changeup, and fastball – along with their corresponding finger angle data patterns. For the knuckleball grip, the fingertips (including the index and middle fingers) rest on top of the ball, with the thumb bent inward underneath, and the fingers curled inward, minimizing spin and creating an unpredictable motion. As the ball is held with the ring and pinky fingertips, these fingers show larger bending angles compared to the index and middle fingers, while the thumb exhibits a greater bending angle compared to other grip types (Figure 5a(i)). By contrast, the changeup grip involves holding the ball deeper in the hand, with more fingers (thumb, index, middle, and ring fingers) wrapped around the ball to reduce speed. As a result, bending angles are consistently lower for all fingers compared to other grip types, reflecting the deep and encompassing hold (Figure 5a(ii)). The fastball grip positions the index and middle fingers along the seams of the ball, with the thumb wrapping around it with small angle to secure the ball and maximize speed and spin. Unlike the knuckleball grip, which uses the fingertips, the

© 2025 Wiley-VCH GmbH

16163028, 2025, 28, Downloaded from https://advanced.onlinelibrary.wiley.com/doi/10.1002/adfm.202502568 by Korea University Medical, Wiley Online Library on [21/07/2025]. See the Terms and Conditions (https://onlinelibrary.wiley.com/terms-and-conditions) on Wiley Online Library for rules of use; OA articles are governed by the applicable Creative Commons License

fastball grip involves using the undersides of the fingers, resulting in overall smaller bending angles. The ring and pinky fingers, not actively involved in gripping the ball, exhibit larger bending angles (Figure 5a(iii)). Distinct grip patterns characterized by unique finger positions form the foundation of the SCMF-based classification system. The system applies SCMF to five fingers to distinguish three grip types in a VR environment (Figure 5b). Each film was connected to the system for data acquisition and capacitance measurement (Figure 5b(i)). Serial port control was used to calibrate data in real time and transmit it to VR environment. Calibration was performed using 80 data points (20 for each of the four angles: 0°, 30°, 60°, 90°) through an ANN linear regression process (Figure 5b(ii)). The output corresponding to finger bending angles was depicted in Figure S22 (Supporting Information) for calibration purposes. The high reliability of the SCMF enabled accurate calibration of film data to finger joint angles in VR through simple linear regression, achieving a calibration accuracy of mean absolute error of 0.00644. Signal samples were collected for each grip type, with 672 (70%) used for training, 144 (15%) used for validation, and 144 (15%) used for test, as shown in Figure 5b. Using the calibrated data, a baseball pitcher's grip classification system, including knuckle, fastball, and changeup grips, was implemented (Figure 5b(iii)). The classification process involved real-time data processing and a 1D CNN algorithm, achieving a classification accuracy of 99.06% (Figure 5b(iv)). Table S2 (Supporting Information) provides details on the process and parameters for constructing the CNN model. When the user held a baseball with the SCMF-attached hand (Figure 5c(i)), the system successfully displayed the type of baseball grip and the hand's posture in the VR environment, visible through the VR glasses (Figure 5c(ii)). A detailed video demonstration can be found in Movie S1 (Supporting Information).

2.6. Application to AR: Workout Monitoring System

Combining AR technology with workout monitoring creates an efficient system that provides immersive visual feedback, allowing users to instantly view the progress and exercise-related information in real time. The integration enhances users' ability to track their performance and potentially prevent injuries through immediate postural corrections. For implementing the described capabilities, an AR workout monitoring system was developed, attaching SCMFs to the chest, shoulders, elbows, and wrists to sense strain and joint bending angles. Throughout the workouts, the chest expands and contracts with each breath. Monitoring whether breathing occurs regularly and on time is important, as proper breathing enhances workout efficiency and helps prevent injuries. During three workouts – arm curl, shoulder press, and side lateral raise – the system displays workout types and provides real-time feedback in an AR environment, guiding users to maintain correct posture. For all workouts, maintaining a neutral wrist position is crucial for correct posture. In arm curls, the elbows increase their bending angle as the forearms lift weights toward the shoulders, focusing on bicep contraction (**Figure 6**a(i)). Shoulder presses involve decreasing the elbow and increasing shoulder bending angle as the shoulders lift weights overhead, emphasizing shoulder and tricep activation (Figure 6a(ii)). The movement of the elbow and shoulder is followed by a controlled increase and decrease, respectively, in bending angles while returning to the original position. Side lateral raises target the side shoulder muscles by increasing the shoulder bending angle to lift the arms laterally to shoulder height (Figure 6a(iii)). Both elbows maintain a consistent, slight bending angle of ≈20°–30° throughout the movement. The exercise concludes with a controlled decrease in the shoulder bending angle to lower the arms back to the starting position. The system captures the body's movements as signals and classifies them to provide accurate feedback and guidance (Figure 6b). After attaching the SCMF to 7 upper body locations (Figure 6b(i)), data acquisition was performed using a capacitance-measuring system that communicated via Bluetooth. The data were transmitted for real-time calibration, preprocessing, and classification before being sent to a smartphone AR application.

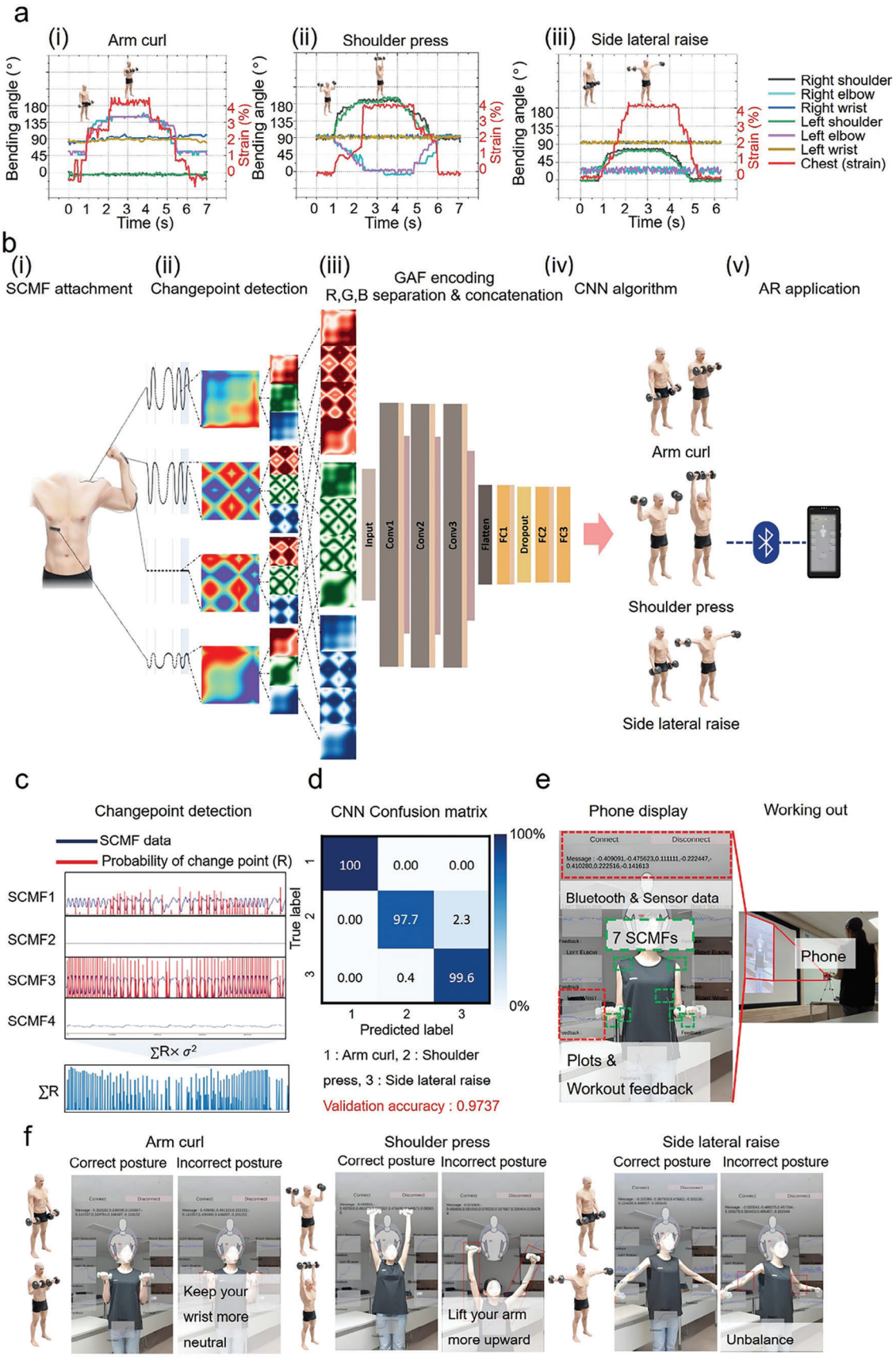
Previous workout monitoring systems segmented workout movements using uniform time windows, limiting monitoring to workouts performed at consistent speeds.[14,17,31,46] To overcome the limitation, a Bayesian change point detection (CPD) algorithm was implemented, enabling real-time, instantaneous time segmentation regardless of workout speed (Figure 6b(ii)).[47] The Bayesian CPD algorithm identifies new data points as change points based on Bayesian probability distributions and previous data. Upon receiving new data, the algorithm calculates the likelihood that this point is a change point using Bayesian methods for prior and posterior predictions. The period between these change points, termed "run length," is then predicted, comparing probabilities to decide if the current point is a change point. Implementing the iterative process allows dynamic segmentation of workout movements based on film data fluctuations. Directly comparing each probability of change point (R) value calculated from the film data uniformly can lead to misinterpreting noise-induced changes as significant changes in trends, resulting in false change point detection. To address this, data normalization and applied weighting were used. Sensor data were normalized, and variances (σ^2) were multiplied by weights to emphasize sensors with significant motions. The weighted R values were summed as $\sum R \times \sigma^2$, which, when exceeding a certain threshold, indicated a change point (Figure 6c).

Upon starting the workout monitoring system and establishing a Bluetooth connection, calibration was performed by receiving 20 stretching and release values from each joint and the chest. To classify arm curl, side lateral raise, and shoulder press workouts, a model was trained. A total of 100 continuous signal samples, representing 100 workout cycles, were collected for each workout. The sample lengths were then augmented to 400 samples per workout using a random time warping method for creating the dataset needed for training the classification model. Random time warping involves stretching and compressing the time series data to create variations randomly. Then, the augmented dataset was randomly segmented, with 50% of the data used for training, 30% for testing, and 20% for validation. Individual film data often pose difficulties in extracting relevant features and patterns for classification. However, combining data from the wrist, shoulder, and elbow improves pattern recognition, enhancing classification accuracy.

Thus, a Gramian angular field (GAF)–CNN algorithm was utilized, processing data using GAF and inputting them into a CNN

© 2025 Wiley-VCH GmbH

16163028, 2025, 28, Downloaded from https://advanced.onlinelibrary.wiley.com/doi/10.1002/adfm.202502568 by Korea University Medical, Wiley Online Library on [21/07/2025]. See the Terms and Conditions (https://onlinelibrary.wiley.com/terms-and-conditions) on Wiley Online Library for rules of use; OA articles are governed by the applicable Creative Commons License



© 2025 Wiley-VCH GmbH

16163028, 2025, 28, Downloaded from https://advanced.onlinelibrary.wiley.com/doi/10.1002/adfm.202502568 by Korea University Medical, Wiley Online Library on [21/07/2025]. See the Terms and Conditions (https://onlinelibrary.wiley.com/terms-and-conditions) on Wiley Online Library for rules of use; OA articles are governed by the applicable Creative Commons License

for classification.[48,49] GAF transforms time series data into 2D images, preserving temporal correlations and enhancing feature extraction. GAF improves classification accuracy and facilitates visualization and interpretation of patterns and anomalies. Initially, segmented data are converted into polar coordinates to generate a Gramian matrix using cosine functions, creating symmetrical 2D images that preserve temporal information. These images are split into R, G, and B channels (Figure 6b(iii)), which are then concatenated into a one big composite image for input into the 2D-CNN (Figure 6b(iv)). The specific CNN architecture can be found in Table S3 (Supporting Information). The method achieved an accuracy of 97.37% (Figure 6d). The combined classification results, which incorporate predicted probabilities, from the 3 SCMFs on the right side and the SCMF on the chest, along with the 3 SCMFs on the left side and the SCMF on the chest, were used to determine the type of workout with the highest overall probability. The film data for joint angles and strain values are transmitted in real time via Bluetooth to a smartphone's AR application, where they are visualized graphically (Figure 6b(v)). After each workout cycle, the application provides the classification result, indicating which workout was performed, and offers feedback on incorrect postures (Figure 6e). When measured values deviate from established thresholds for each joint, the application provides specific posture correction instructions, such as "keep your wrist neutral" or "lift your arm upward," guiding the user back to the correct posture.

Figure 6f provides an illustration and the results of the entire AR workout monitoring system, showing how SCMF is attached and feedback is provided as the user performs three different exercises using the AR application. Users can see their movements through display while simultaneously receiving immediate feedback on their posture and joint movements directly on the display. Incorrect posture data and feedback can be found in Figure S23 (Supporting Information). A detailed video demonstration is also available in Movie S2 (Supporting Information).

3. Conclusions

A SCMF was developed with an adhesion layer comprising a high-adhesion elastomer matrix incorporating PEIE, designed for better skin attachment and signal reliability. The SCMF's high conformality to skin movements forms the basis for precise motion tracking, resulting in reliable strain and bending angle signals. Real-time integration and increased utility are achieved through accurate calibration. Furthermore, the accurately calibrated data enable real-time monitoring and motion classification in AR and VR environments through CNN algorithms. Integration of the capabilities enhances the functionality of immersive systems, demonstrating SCMF's potential to significantly improve motion tracking and user interaction in VR and AR technologies compared to previous research approaches (Table S4, Supporting Information).

Despite the advancements, areas for further improvement have been identified. While the achieved gauge factor has proven sufficient for targeted applications, future implementations may require enhanced sensitivity for more precise motion detection, which could be achieved through micro/nanostructuring of the dielectric layer.[50–52] Excessive sweating can weaken the interaction between the film and the skin, leading to reduced adhesion. Microstructuring can offer a solution by forming precise micropatterns on the film surface, which increase the contact area and strengthen the physical bond, while also enhancing resistance to environmental factors such as sweat.[53–60] Implementing a hierarchical structure of micro- and nanoscale patterns could increase the surface area and induce a capillary effect. The approach may improve sweat management and maintain adhesion under high-moisture conditions, addressing limitations caused by perspiration. Additionally, the current wired system may generate noise due to capacitance changes from contact between wires and reduce user convenience. Implementing NFC wireless communication could address these issues. By attaching NFC tags to exercise equipment and incorporating coils into the films, wireless AR applications could be enabled in settings such as gyms, enhancing usability and expanding potential applications.[61–64] The wireless integration could potentially reduce the system's overall weight and complexity, leading to improved user comfort and longer wear times. Additionally, future research may focus on algorithms for complex motion recognition, system miniaturization, and integration with other sensing modalities. Combining SCMF with EMG or IMU sensors could provide a broader view of user movements. Exploring biocompatible materials for the adhesive layer may increase wear duration, supporting extended health monitoring applications.

Overall, the SCMF represents a significant contribution to immersive technology, balancing accuracy, comfort, and cost-effectiveness (Table S5, Supporting Information). Its seamless integration with current VR and AR systems enhances user experiences across diverse applications, opening new possibilities in entertainment, healthcare, fitness monitoring, and gesture-based controls.

4. Experimental Section

SCMF Fabrication: A CNT (MR99, Carbon Nano-material Technology Co., Ltd., Republic of Korea) dispersion was prepared by dispersing 0.1 g of CNT in 50 g of isopropyl alcohol (Daejung Chemicals, Republic of Korea) using a tip sonicator (VCX 750, Sonics & Materials, USA) at 100 W for 40 min. The CNT solution was spray-coated onto a preheated silicon

Figure 6. Demonstration of SCMF application for workout monitoring system in AR. a) SCMF signals from seven upper body locations (left and right shoulders, elbows, wrists, and chest) during three types of workouts: i) arm curl, ii) shoulder press, and iii) side lateral raise. b) Overview of the AR workout monitoring system process. i) Attaching SCMF to all seven upper body locations and ii) using a change point detection process to segment each workout cycle. iii) Preprocessing time series data for classification using GAF and combining four SCMF signals into a single input through RGB separation and concatenation. iv) CNN architecture for classifying arm curl, shoulder press, and side lateral raise. v) Execution of the workout monitoring system in a smartphone AR application. c) Process of detecting change points using the change point detection probability and weighing it with variance from four SCMF. d) Confusion matrix of the classification results, with a validation accuracy of 0.9737. e) Demonstration of the workout monitoring process using the AR application, including the smartphone display during the workout. f) Real-time classification results of the three types of workouts and joint feedback in the AR application. Smartphone display showing correct and incorrect posture for each workout.

© 2025 Wiley-VCH GmbH

16163028, 2025, 28, Downloaded from https://advanced.onlinelibrary.wiley.com/doi/10.1002/adfm.202502568 by Korea University Medical, Wiley Online Library on [21/07/2025]. See the Terms and Conditions (https://onlinelibrary.wiley.com/terms-and-conditions) on Wiley Online Library for rules of use; OA articles are governed by the applicable Creative Commons License

16163028, 2025, 28, Downloaded from https://advanced.onlinelibrary.wiley.com/doi/10.1002/adfm.202502568 by Korea University Medical, Wiley Online Library on [21/07/2025]. See the Terms and Conditions (https://onlinelibrary.wiley.com/terms-and-conditions) on Wiley Online Library for rules of use; OA articles are governed by the applicable Creative Commons License

wafer (525 µm thickness, University Wafer, USA) on a 160 °C hot plate, repeating the process 5 times to ensure uniform coating. An Ecoflex mixture (Ecoflex 00-30, Smooth-On, Inc., USA) was spin-coated over the CNT layer at 150 rpm for 1 min, then cured at 60 °C for 30 min. During curing, the CNTs became embedded in the Ecoflex matrix. The cured film, with CNTs embedded, was peeled off from the wafer and cut to size. A 24 gauge wire (AWG24, Dongguan City Yason General Machinery Co., China) was attached to the CNT surface using silver epoxy (CW2400, Chemtronics, USA) and cured at room temperature for 24 h. For the second layer, Ecoflex was mixed with 1.32 wt% PEIE (Sigma-Aldrich, USA) and processed similarly. The two films were bonded using a thin layer of Ecoflex, cured at 60 °C for 30 min, with the PEIE-coated film placed on the bottom.

Adhesion Characteristic Test:

1) Peel tests were conducted using a universal testing machine (UTM) (AGS-X (1 kN), Shimadzu Corporation, Japan) combined with a customized linear stage moving at a constant speed of 12 mm s^{-1}. The tests were performed on both human skin and porcine skin substrates. For the porcine skin, Micropig Franz Cell Membrane (APURES Corporation) was used. The adhesive films were applied to the substrates with consistent pressure to ensure uniform adhesion. Peel strength was measured by applying a perpendicular force to the adhesive interface, recording the force required to peel the film from the substrate. The testing parameters, such as peel angle (90°) and rate, were controlled to maintain consistency across trials. Data acquisition was synchronized with the UTM to accurately capture force–displacement curves, allowing for the analysis of peel strength and adhesive failure modes.
2) Surface microwrinkles were imaged using a scanning electron microscope (SEM) (S-4800, HITACHI). The samples were mounted on aluminum stubs using conductive carbon tape and sputter-coated with a thin layer of platinum (≈5 nm) to enhance conductivity and prevent charging. SEM images were acquired at an accelerating voltage of 5 kV with a working distance of 10 mm. The surface morphology and microwrinkle structures were analyzed at various magnifications ranging from 500× to 10 000× to capture detailed features of the topography.
3) The 1H-NMR spectra were recorded using a Bruker, AVANCE III 300 NMR spectrometer operating at 300 MHz. The sample was prepared by dissolving the analyte in deuterated chloroform, which was used as the solvent and internal reference (δ = 7.26 ppm). The spectra were acquired at room temperature under standard conditions with a spectral width of 4000 Hz, 16 scans, and a relaxation delay of 1.0 s to ensure complete relaxation between pulses. The obtained data were processed and analyzed using Bruker's TopSpin software.
4) To simulate the effects of sweat on adhesive performance, distilled water was sprayed onto porcine skin substrates until the surface was wetted. The water was allowed to absorb into the skin for 10 min to mimic the natural process of sweat absorption into human skin, ensuring a realistic representation of perspiration conditions. Peel tests were then conducted immediately afterward to quantitatively evaluate the adhesive's performance. For real-world sweating evaluation, the SCMF was attached to a wrist during a 30 min running session, followed by immediate comparative testing of wrist motion measurements to assess performance under pre- and postexercise conditions.
5) For dust contamination testing, a two-phase process was employed. First, dust was collected in an open-top plastic chamber placed in the laboratory for over 30 days, allowing for natural accumulation. The film samples were then adhered to and immediately detached from the accumulated dust layer, simulating dust exposure. Subsequently, the samples were exposed to additional dust accumulation for 7 days in a controlled laboratory environment. Following this extended exposure to the high-particulate environment, the films were subsequently cleaned using an ultrasonic bath sonicator (40 kHz, 100 W) for 10 or 30 min in deionized water or ethanol. Peel strength tests were carried out both before and after cleaning to assess the impact of dust contamination and the effectiveness of the cleaning process in restoring adhesive performance.
6) To evaluate adhesion characteristics under varying pH conditions representative of human skin (pH 4–6), pH-controlled tests were performed on porcine skin substrates. The test solutions were prepared using buffer solutions and ascorbic acid to achieve precise pH values of 4, 5, and 6. These solutions were applied to the porcine skin surface and allowed to fully interact with the substrate for 10 min before testing. Peel tests were then conducted using the same UTM setup and parameters as described in the standard adhesion tests. This methodology enabled the assessment of adhesive performance across the physiologically relevant pH range typically found on human skin.

SCMF Characteristic Test: For the characteristic test, capacitance measurements were performed under various applied strains and bending angles. A customized linear stage was used to apply precise strains to the SCMF samples, while a commercial LCR meter (E4980A, Agilent, USA) was employed to measure capacitance. Strain was applied incrementally, with measurements taken at each strain point to evaluate the SCMF's responsiveness. Additionally, a customized setup was designed to control and measure different bending angles, ranging from 0° to 70°. The bending angle was gradually adjusted in small increments, and capacitance values were recorded at each angle to study the effect of bending on the electrical characteristics of the SCMF. Data acquisition was synchronized with the strain and bending angle adjustments to ensure accurate correlation between mechanical deformation and capacitance change.

VR and AR Systems:

1) For the VR system, capacitance changes in the SCMF were measured using an MPR121 board, which was connected to an Arduino Mega board. The data were communicated in real time from the Arduino to a computer via serial communication. Calibration and classification results were processed using Python, and the processed data were then transmitted back to the Arduino Mega board through serial communication. The data were further sent to Unity, where a predesigned baseball game environment was developed.
2) For the AR system, capacitance changes in the SCMF were measured similarly using an MPR121 board connected to an Arduino Mega board and an HC-05 Bluetooth module. The capacitance data were transmitted via Bluetooth to another Arduino Mega and HC-05 module connected to a computer, which processed the data using Python for calibration and classification. The processed results were then communicated to a smartphone through Bluetooth. A custom AR application, built using Unity AR, provided a user interface for workout monitoring, allowing real-time feedback and interaction with the SCMF-based input system.

All experiments involving human participants were conducted in compliance with ethical standards and were approved by the KAIST Institutional Review Board. Written informed consent was obtained from all participants prior to their involvement in the study.

Supporting Information

Supporting Information is available from the Wiley Online Library or from the author.

Acknowledgements

I.P. was supported by the National Research Foundation of Korea (NRF) grant funded by the Korean government (MSIT, Grant No. 2021R1A2C3008742); the Alchemist Project grant funded by the Korea Evaluation Institute of Industrial Technology (KEIT) & the Korea Government (MOTIE) (Project numbers: 1415179744, 20019169). J.A. was supported by the KEIT grant funded by the Korea government (MOTIE,

 © 2025 Wiley-VCH GmbH

Grant No. RS-2022-00154781, development of large-area wafer-level flexible/stretchable hybrid sensor platform technology for form-factor-free highly integrated convergence sensor).

Conflict of Interest

The authors declare no conflict of interest.

Data Availability Statement

The data that support the findings of this study are available from the corresponding author upon reasonable request.

Keywords

augmented reality (AR), motion monitoring film, skin-conformal sensor, virtual reality (VR), workout monitoring

Received: January 26, 2025
Published online: February 24, 2025

[1] M. Gopakumar, G. Y. Lee, S. Choi, B. Chao, Y. Peng, J. Kim, G. Wetzstein, *Nature* **2024**, *629*, 791.
[2] W. Yang, S. Lin, W. Gong, R. Lin, C. Jiang, X. Yang, Y. Hu, J. Wang, X. Xiao, K. Li, Y. Li, Q. Zhang, J. S. Ho, Y. Liu, C. Hou, H. Wang, *Science* **2024**, *384*, 74.
[3] S. Luo, M. Jiang, S. Zhang, J. Zhu, S. Yu, I. D. Silva, T. Wang, E. Rouse, B. Zhou, H. Yuk, X. Zhou, H. Su, *Nature* **2024**, *630*, 353.
[4] M. Zhu, Z. Sun, Z. Zhang, Q. Shi, T. He, H. Liu, T. Chen, C. Lee, *Sci. Adv.* **2020**, *6*, aaz869.
[5] L. Li, S. Zhao, W. Ran, Z. Li, Y. Yan, B. Zhong, Z. Lou, L. Wang, G. Shen, *Nat. Commun.* **2022**, *13*, 5975.
[6] Y. Liu, C. K. Yiu, Z. Zhao, W. Park, R. Shi, X. Huang, Y. Zeng, K. Wang, T. H. Wong, S. Jia, J. Zhou, Z. Gao, L. Zhao, K. Yao, J. Li, C. Sha, Y. Gao, G. Zhao, Y. Huang, D. Li, Q. Guo, Y. Li, X. Yu, *Nat. Commun.* **2023**, *14*, 2297.
[7] K. Kim, H. Yang, J. Lee, W. G. Lee, *Adv. Sci.* **2023**, *10*, 2303234.
[8] Q. Liang, D. Zhang, T. He, Z. Zhang, Y. Wu, G. Zhang, R. Xie, S. Chen, H. Wang, C. Lee, *Nano Energy* **2023**, *117*, 108903.
[9] Y. Lee, B. Jang, H. Song, S. Kim, Y. Won Kwon, S. Kang, M. S. Kim, I. Park, T.-S. Kim, J. Jang, J.-H. Kim, J.-U. Park, B.-S. Bae, *Nat. Commun.* **2024**, *15*, 7146.
[10] J. Kim, A. S. Campbell, B. E. F. de Ávila, J. Wang, *Nat. Biotechnol.* **2019**, *37*, 389.
[11] F. Wen, Z. Sun, T. He, Q. Shi, M. Zhu, Z. Zhang, L. Li, T. Zhang, C. Lee, *Adv. Sci.* **2020**, *7*, 2000261.
[12] B. Ji, X. Wang, Z. Liang, H. Zhang, Q. Xia, L. Xie, H. Yan, F. Sun, H. Feng, K. Tao, Q. Shen, E. Yin, *Int. J. Hum. Comput. Interact.* **2023**, *39*, 6793.
[13] K. K. Kim, M. Kim, K. Pyun, J. Kim, J. Min, S. Koh, S. E. Root, J. Kim, B. N. T. Nguyen, Y. Nishio, S. Han, J. Choi, C. Y. Kim, J. B. H. Tok, S. Jo, S. H. Ko, Z. Bao, *Nat. Electron.* **2023**, *6*, 64.
[14] K. K. Kim, I. H. Ha, M. Kim, J. Choi, P. Won, S. Jo, S. H. Ko, *Nat. Commun.* **2020**, *11*, 2149.
[15] A. Miyamoto, S. Lee, N. F. Cooray, S. Lee, M. Mori, N. Matsuhisa, H. Jin, L. Yoda, T. Yokota, A. Itoh, M. Sekino, H. Kawasaki, T. Ebihara, M. Amagai, T. Someya, *Nat. Nanotechnol.* **2017**, *12*, 907.
[16] H. Cho, I. Lee, J. Jang, J. H. Kim, H. Lee, S. Park, G. Wang, *Nat. Electron.* **2023**, *6*, 619.
[17] S. Wang, Y. Fang, H. He, L. Zhang, C. Li, J. Ouyang, *Adv. Funct. Mater.* **2021**, *31*, 2007495.
[18] J. Gu, D. Kwon, J. Ahn, I. Park, *ACS Appl. Mater. Interfaces* **2020**, *12*, 10908.
[19] C. Wei, R. Cheng, C. Ning, X. Wei, X. Peng, T. Lv, F. Sheng, K. Dong, Z. L. Wang, *Adv. Funct. Mater.* **2023**, *33*, 2303562.
[20] L. Sanchez-Botero, A. Agrawala, R. Kramer-Bottiglio, *Adv. Mater. Technol.* **2023**, *8*, 2300378.
[21] Z. Sun, C. Dong, B. Chen, W. Li, H. Hu, J. Zhou, C. Li, Z. Huang, *Small* **2023**, *19*, 2303612.
[22] M. Salauddin, S. M. S. Rana, M. Sharifuzzaman, H. S. Song, M. S. Reza, S. H. Jeong, J. Y. Park, *Adv. Energy Mater.* **2023**, *13*, 2203812.
[23] J. Ahn, S. Cho, L. Wu, X. Li, D. Lee, J.-H. Ha, H. Han, K. Lee, B. Kang, Y. Kwon, S. H. Hwang, S. Jeon, B. Yu, J. Ahn, J.-H. Jeong, I. Park, *Nano Energy* **2024**, *129*, 110045.
[24] J. Gu, J. Ahn, J. Jung, S. Cho, J. Choi, Y. Jeong, J. Park, S. Hwang, I. Cho, J. Ko, J. H. Ha, Z. J. Zhao, S. Jeon, S. Ryu, J. H. Jeong, I. Park, *Nano Energy* **2021**, *89*, 106447.
[25] Y. Jung, J. Gu, J. Yeo, W. Lee, H. Han, J. Choi, J.-H. Ha, J. Ahn, H. Cho, S. Ryu, I. Park, *Small* **2024**, *20*, 2303981.
[26] M. S. Kim, Y. Lee, J. Ahn, S. Kim, K. Kang, H. Lim, B. S. Bae, I. Park, *Adv. Funct. Mater.* **2023**, *33*, 2208792.
[27] Z. Chen, Y. Ma, H. Wang, B. Yu, L. Qian, Z. J. Zhao, *Chem. Eng. J.* **2024**, *497*, 154953.
[28] R. Madhavan, *Mater. Adv.* **2022**, *3*, 8665.
[29] R. Madhavan, *New J. Chem.* **2022**, *46*, 17596.
[30] R. Madhavan, *Macromol. Mater. Eng.* **2022**, *307*, 2200034.
[31] Y. Jeong, J. Gu, J. Byun, J. Ahn, J. Byun, K. Kim, J. Park, J. Ko, J.-h. Jeong, M. Amjadi, I. Park, *Adv. Healthcare Mater.* **2021**, *10*, 2001461.
[32] J. H. Lee, K. Cho, J. K. Kim, *Adv. Mater.* **2024**, *36*, 2310505.
[33] X. Yu, Z. Xie, Y. Yu, J. Lee, A. Vazquez-Guardado, H. Luan, J. Ruban, X. Ning, A. Akhtar, D. Li, B. Ji, Y. Liu, R. Sun, J. Cao, Q. Huo, Y. Zhong, C. M. Lee, S. Y. Kim, P. Gutruf, C. Zhang, Y. Xue, Q. Guo, A. Chempakasseril, P. Tian, W. Lu, J. Y. Jeong, Y. J. Yu, J. Cornman, C. S. Tan, B. H. Kim, et al., *Nature* **2019**, *575*, 473.
[34] S. H. Jeong, S. Zhang, K. Hjort, J. Hilborn, Z. G. Wu, *Adv. Mater.* **2016**, *28*, 5830.
[35] X. Wan, Z. Gu, F. Zhang, D. Hao, X. Liu, B. Dai, Y. Song, S. Wang, *NPG Asia Mater.* **2019**, *11*, 49.
[36] P. Zhang, W. Zhou, Y. He, Z. Xu, M. Li, W. Hong, C. Yang, *ACS Appl. Mater. Interfaces* **2022**, *14*, 49264.
[37] Z. Gu, X. Wan, Z. Lou, F. Zhang, L. Shi, S. Li, B. Dai, G. Shen, S. Wang, *ACS Appl. Mater. Interfaces* **2019**, *11*, 1496.
[38] Y. Zhou, L. Yang, Z. Liu, Y. Sun, J. Huang, B. Liu, Q. Wang, L. Wang, Y. Miao, M. Xing, Z. Hu, *Sci. Adv.* **2023**, *9*, eadf1043.
[39] H. Min, S. Baik, J. Lee, D. W. Kim, J. H. Song, K. H. Kim, M. S. Kim, C. Pang, *Chem. Eng. J.* **2022**, *429*, 132467.
[40] N. T. Vargas, C. L. Chapman, B. D. Johnson, R. Gathercole, Z. J. Schlader, *Am. J. Physiol.: Regul., Integr. Comp. Physiol.* **2018**, *315*, R925.
[41] T. Hu, B. Sheng, *ACS Appl. Mater. Interfaces* **2024**, *16*, 21061.
[42] T. Yamada, Y. Hayamizu, Y. Yamamoto, Y. Yomogida, A. Izadi-Najafabadi, D. N. Futaba, K. Hata, *Nat. Nanotechnol.* **2011**, *6*, 296.
[43] L. Cai, L. Song, P. Luan, Q. Zhang, N. Zhang, Q. Gao, D. Zhao, X. Zhang, M. Tu, F. Yang, W. Zhou, Q. Fan, J. Luo, W. Zhou, P. M. Ajayan, S. Xie, *Sci. Rep.* **2013**, *3*, srep03402.
[44] H. N. Hs. O. I. H., F. K. Tokiya Yamaji, *J. Sens.* **2017**, 9893758.
[45] N. Ni, *Alexandria Eng. J.* **2021**, *60*, 5991.
[46] J. Lee, S. Kim, J. Lee, D. Yang, B. C. Park, S. Ryu, I. Park, *Nanoscale* **2014**, *6*, 11932.
[47] R. P. Adams, D. J. C. MacKay, arXiv **2007**, 10703742.
[48] C. L. Yang, Z. X. Chen, C. Y. Yang, *Sensors* **2020**, *20*, 168.

 © 2025 Wiley-VCH GmbH

16163028, 2025, 28, Downloaded from https://advanced.onlinelibrary.wiley.com/doi/10.1002/adfm.202502568 by Korea University Medical, Wiley Online Library on [21/07/2025]. See the Terms and Conditions (https://onlinelibrary.wiley.com/terms-and-conditions) on Wiley Online Library for rules of use; OA articles are governed by the applicable Creative Commons License

[49] Y. Sharma, N. Coronato, D. E. Brown, presented at 2022 44th Annual Int. Conf. IEEE E Medicine Biology Society (EMBC), Glasgow, Scotland, UK, July **2022**.
[50] X. He, B. Zhang, Q. Liu, H. Chen, J. Cheng, B. Jian, H. Yin, H. Li, K. Duan, J. Zhang, Q. Ge, *Nat. Commun.* **2024**, *15*, 6431.
[51] R. Yang, A. Dutta, B. Li, N. Tiwari, W. Zhang, Z. Niu, Y. Gao, D. Erdely, X. Xin, T. Li, H. Cheng, *Nat. Commun.* **2023**, *14*, 2907.
[52] X. He, Z. Liu, G. Shen, X. He, J. Liang, Y. Zhong, T. Liang, J. He, Y. Xin, C. Zhang, D. Ye, G. Cai, *npj Flexible Electron.* **2021**, *5*, 17.
[53] J. Ahn, Z. J. Zhao, J. Choi, Y. Jeong, S. Hwang, J. Ko, J. Gu, S. Jeon, J. Park, M. Kang, D. V. Del Orbe, I. Cho, H. Kang, M. Bok, J. H. Jeong, I. Park, *Nano Energy* **2021**, *85*, 105978.
[54] J. Ahn, H. Han, J. H. Ha, Y. Jeong, Y. Jung, J. Choi, S. Cho, S. Jeon, J. H. Jeong, I. Park, *Adv. Mater.* **2024**, *36*, 2300871.
[55] J. Ahn, J. H. Ha, Y. Jeong, Y. Jung, J. Choi, J. Gu, S. H. Hwang, M. Kang, J. Ko, S. Cho, H. Han, K. Kang, J. Park, S. Jeon, J. H. Jeong, I. Park, *Nat. Commun.* **2023**, *14*, 833.
[56] J. H. Oh, S. Y. Hong, H. Park, S. W. Jin, Y. R. Jeong, S. Y. Oh, J. Yun, H. Lee, J. W. Kim, J. S. Ha, *ACS Appl. Mater. Interfaces* **2018**, *10*, 7263.
[57] S. Baik, H. J. Lee, D. W. Kim, J. W. Kim, Y. Lee, C. Pang, *Adv. Mater.* **2019**, *31*, 1803309.
[58] H. Park, C. Song, S. W. Jin, H. Lee, K. Keum, Y. H. Lee, G. Lee, Y. R. Jeong, J. S. Ha, *Nano Energy* **2021**, *83*, 105837.
[59] S. Baik, J. Kim, H. J. Lee, T. H. Lee, C. Pang, *Adv. Sci.* **2018**, *5*, 1800100.
[60] S. Chun, D. W. Kim, S. Baik, H. J. Lee, J. H. Lee, S. H. Bhang, C. Pang, *Adv. Funct. Mater.* **2018**, *28*, 1805224.
[61] H. Han, H. Park, S. Cho, S.-U. Lee, J. Choi, J.-H. Ha, J. Park, Y. Jung, H. Kim, J. Ahn, J. Kwon, Y. S. Oh, M. Je, I. Park, *Small* **2024**, *20*, 2405493.
[62] S. Cho, H. Han, H. Park, S. U. Lee, J. H. Kim, S. W. Jeon, M. Wang, R. Avila, Z. Xi, K. Ko, M. Park, J. Lee, M. Choi, J. S. Lee, W. G. Min, B. J. Lee, S. Lee, J. Choi, J. Gu, J. Park, M. S. Kim, J. Ahn, O. Gul, C. Han, G. Lee, S. Kim, K. Kim, J. Kim, C. M. Kang, J. Koo, et al., *npj Flexible Electron.* **2023**, *7*, 8.
[63] S. Cho, J. H. Ha, J. Ahn, H. Han, Y. Jeong, S. Jeon, S. Hwang, J. Choi, Y. S. Oh, D. Kim, S. A. Park, D. Lee, J. Ahn, B. Kang, B. H. Kang, J. H. Jeong, I. Park, *Adv. Funct. Mater.* **2024**, *34*, 2316196.
[64] Y. S. Oh, J. H. Kim, Z. Xie, S. Cho, H. Han, S. W. Jeon, M. Park, M. Namkoong, R. Avila, Z. Song, S. U. Lee, K. Ko, J. Lee, J. S. Lee, W. G. Min, B. J. Lee, M. Choi, H. U. Chung, J. Kim, M. Han, J. Koo, Y. S. Choi, S. S. Kwak, S. B. Kim, J. Kim, J. Choi, C. M. Kang, J. U. Kim, K. Kwon, S. M. Won, et al., *Nat. Commun.* **2021**, *12*, 5008.

© 2025 Wiley-VCH GmbH

16163028, 2025, 28, Downloaded from https://advanced.onlinelibrary.wiley.com/doi/10.1002/adfm.202502568 by Korea University Medical, Wiley Online Library on [21/07/2025]. See the Terms and Conditions (https://onlinelibrary.wiley.com/terms-and-conditions) on Wiley Online Library for rules of use; OA articles are governed by the applicable Creative Commons License